EES Catalysis

ROYAL SOCIETY OF CHEMISTRY

PAPER

View Article Online
View Journal | View Issue

Open Access Article. Published on 20 Januari 2024. Downloaded on 8/13/2025 6:22:11 AM.
This article is licensed under a Creative Commons Attribution-NonCommercial 3.0 Unported Licence.

Check for updates

Cite this: *EES Catal.*, 2024, 2, 811

Photothermal catalytic oxidation of toluene over the Pt–Mn_2O_3/CN nanocomposite catalyst†

Xiao Yu,‡[abc] Chuang Zhao,‡[c] Lixia Yang, *[c] Jian Zhang *[ab] and Chunlin Chen *[ab]

Received 6th December 2023,
Accepted 18th January 2024

DOI: 10.1039/d3ey00298e

rsc.li/eescatalysis

The Pt–Mn_2O_3/CN catalyst formed through synthesis *via* a solvent-thermal method involves a synergistic combination of polymer CN and Pt nanoparticles loaded on Mn_2O_3 to catalyze the degradation of toluene. The composition incorporates Mn_2O_3 as the central element for photothermal conversion, CN as a uniformly dispersed matrix for Pt nanoparticles, and Pt as the catalytically active center, demonstrating significant efficacy. Particularly noteworthy is the discernible enhancement in the photothermal catalytic degradation capability of the Pt–Mn_2O_3/CN composite catalyst, specifically in the context of toluene. When subjected to light intensity of 300 mW cm^{-2} and a toluene concentration of 400 ppm, Pt–Mn_2O_3/CN achieves toluene conversion and CO_2 mineralization rates of 99% and 80.9%, respectively. This improvement primarily stems from the Pt nanoparticles inducing a substantial presence of oxygen vacancies within the catalyst structure, thereby increasing the oxygen adsorption capacity and surface mobility. This, in turn, activates adsorbed oxygen species at the catalyst's interface. The adept utilization and conversion of solar irradiance for volatile organic compound (VOC) abatement underscore its potential as an environmentally friendly and renewable energy source.

Broader context

In recent years, significant strides have been made in advancing photothermal catalysis – an innovative technology harnessing solar energy to enhance catalytic efficiency through synergistic photothermal effects. Toluene, classified as a volatile organic compound (VOC), poses a threat to air quality, potentially contributing to ground-level ozone and smog formation when released into the atmosphere. Exploring renewable solar power *via* photothermal catalysis emerges as a promising avenue to combat VOC-related environmental concerns. In our investigation, we synthesized a nanocomposite catalyst by combining polymer CN with Pt nanoparticles strategically loaded onto Mn_2O_3. This catalyst demonstrated remarkable efficiency in the photothermal catalytic oxidation of toluene, credited to the Pt nanoparticles inducing numerous oxygen vacancies within the catalyst structure. These vacancies notably amplified the oxygen adsorption capacity, enhanced surface fluidity, and activated adsorbed oxygen on the catalyst's surface. Our research holds the promise of significant environmental advantages, highlighting the potential of utilizing sunlight as a clean and sustainable energy source for degrading VOCs.

Introduction

Toluene (C_7H_8) is commonly known as methylbenzene. Inhalation of toluene presents health risks, with prolonged exposure to its vapors causing symptoms such as headaches, dizziness, and in severe instances, damage to the central nervous system.[1] Categorized as a volatile organic compound (VOC), toluene contributes to air pollution, potentially leading to the formation of ground-level ozone and smog when released into the atmosphere.[2] In recent developments, photothermal catalysis has emerged as an advanced and promising technology for the removal of VOCs from the air.[3] This innovative approach combines light-induced heating with catalytic processes to either eliminate or transform VOCs. Numerous studies have highlighted the superior catalytic activity of photothermal catalysis in VOC degradation. This efficacy is attributed to the synergistic interaction between photocatalysis and thermal catalysis.[4] For example, research conducted by Jia's team showcased the potential of Pt–rGO–TiO_2 as a highly active photothermal catalyst for VOC decomposition. This catalyst demonstrated broad light wavelength absorption and

---

[a] *Ningbo Institute of Materials Technology & Engineering, Chinese Academy of Sciences, 1219 Zhongguan West Road, Ningbo 315201, Zhejiang, China*
[b] *University of Chinese Academy of Sciences, Beijing 100049, China*
[c] *Key Laboratory of Jiangxi Province for Persistent Pollutants Control and Resources Recycle, Nanchang Hangkong University, Nanchang 330063, Jiangxi Province, China*

† Electronic supplementary information (ESI) available. See DOI: **https://doi.org/10.1039/d3ey00298e**

‡ These authors contributed equally.

© 2024 The Author(s). Published by the Royal Society of Chemistry

Open Access Article. Published on 20 Januwari 2024. Downloaded on 8/13/2025 6:22:11 AM.
This article is licensed under a Creative Commons Attribution-NonCommercial 3.0 Unported Licence.

solar-thermal synergy effect.[5] Additionally, they synthesized Pt-mTiO_2/USY composites for the catalytic degradation of toluene under the full solar spectrum. The mTiO_2/USY with increasing Pt content exhibited progressively enhanced catalytic activity, indicating the promising nature of these materials in VOC removal applications.[6]

Catalysts based on manganese oxide are widely employed in environmental catalysis due to their affordability, abundant sources, and variable valence states.[7,8] However, manganese oxide has a relatively wide band gap, which may limit its efficiency in utilizing sunlight for photothermal catalysis. To enhance catalysts' reactivity, researchers have confirmed that heteroatom loading, which regulates the electronic structure and improves light absorption, is an effective strategy.[9,10] Moreover, the lattice defects of metal oxides can be altered by loading heteroatoms, facilitating the generation of more reactive oxygen species and thereby improving catalytic activity.[11] Some research also found that the dispersion of metal ions and the augmentation of the active sites are enhanced when metal oxides or noble metals are supported on flat materials.[12] Polymeric carbon nitrides (CN), composed of triazine or heptazine units as building blocks, present a promising class of conjugated polymeric photocatalyst for exploring this possibility.[13] Similar to graphite, CN monolayers are stacked with van der Waals force interactions, rendering them insoluble in most solvents. CN has emerged as an exceptionally attractive photocatalyst driven by visible light, distinguishing it from TiO_2 materials that are responsive only to UV light (representing just 5% of the solar spectrum). With a suitable forbidden bandwidth (E_g = 2.7–2.8 eV), CN exhibits superior absorption of visible light compared to most metal oxides.[14] It is particularly well-suited for the photocatalytic decomposition of water to generate hydrogen and oxygen.

Wang *et al.* initially reported on CN's visible light photocatalytic water decomposition for hydrogen production, marking a shift in photocatalyst research from inorganic semiconductors to diverse organic polymers.[15] In a study by Zhang *et al.*,[16] it was demonstrated that carbon nitride, characterized by excellent light-response capabilities and a layered structure, serves to prevent nanoparticle aggregation and resist chemical corrosion from acids and organic solvents. Additionally, CN can be synergistically combined with metal oxides to modulate the electronic structure of the composite catalyst. The nitrogen atoms in CN play a crucial role by providing lone pair electrons as ligands to the transition metal, contributing to the overall regulation of the catalyst's electronic structure.[17] Moreover, metal nanoparticles demonstrate outstanding activity in photo-driven photothermal catalysis, often credited to the presence of hot electrons generated by the robust surface plasmon resonance (SPR) effect. Professor Zhang's research team delved into the innovative photothermal Fischer–Tropsch synthesis employing the RuCo-SAA alloy catalyst, affirming a promising approach for converting carbon monoxide into high-value chemicals.[18] Additionally, their findings highlighted the beneficial role of plasmonic Cu nanoparticles in enhancing the low-temperature photo-driven water–gas shift reaction.[19]

Herein, we synthesized a Pt–Mn_2O_3/CN nanocomposite catalyst *via* loading the Pt and combining CN into Mn_2O_3 by a solvent-thermal method. This investigation focuses on utilizing Pt nanoparticles (NPs) as active sites, Mn_2O_3 as the center for photothermal conversion, and CN as a dispersed material to facilitate the even distribution of Pt nanoparticles. The multicatalytic system is employed to investigate the mechanism behind the enhanced photothermal catalytic degradation of toluene by doping Pt NPs. The findings reveal that the Pt–Mn_2O_3/CN catalyst harnesses solar energy to activate active oxygen species on the surface of oxygen vacancies, enhancing the catalyst's stability through the robust interaction between CN and Mn_2O_3. This discovery holds significant potential for widespread applications in the photothermal catalytic degradation of VOCs.

Results and discussion

Structural information of the catalysts

As depicted in the XRD spectra of various catalysts presented in Fig. 1A, these catalyst formulations exhibit nearly identical diffraction patterns to the pristine Mn_2O_3. The distinct peaks at 66.2°, 55.3°, 49.5°, 45.5°, 38.8°, 33.1°, and 23.3° correspond to the crystallographic planes of (622), (440), (431), (332), (400), (222), and (211), respectively, all indexed to Mn_2O_3.[10] Notably, the Pt–Mn_2O_3/CN catalyst shows no discernible diffraction peaks associated with the CN structure or Pt nanoparticles. This observation suggests that the catalyst predominantly consists of Mn_2O_3, a phenomenon likely attributable to the low Pt loading or the effective dispersion of small-size Pt NPs. However, an intriguing phenomenon is observed in the enlarged diffraction peaks at 33.1°, as illustrated in Fig. 1A (left), corresponding to the (222) crystal in Mn_2O_3 undergoing a negative shift. This implies an expansion of the lattice spacings along the c direction, indicating the incorporation of a fraction of CN and Pt NPs into the Mn_2O_3 lattice during catalyst synthesis. In this context, the thermal oxidation process's heating treatment is presumed to promote a more compact packing of CN or Pt NPs, thereby leading to an expansion of the lattice distance.[20]

The examination delved into the N_2 adsorption–desorption isotherm and the distribution of pore sizes among diverse catalyst samples. As depicted in Fig. 1B, only Pt–Mn_2O_3/CN and Mn_2O_3/CN samples exhibit typical type IV isotherms characterized by the H3 hysteresis ring,[21] signifying the existence of a mesoporous structure owing to the layering effects within CN. From the BET and BJH models, values for specific surface area, pore volume, and pore size were computed, as outlined in Table 1. As the CN content in the catalyst increased, the S_{BET} surged from 11.01 to 17.68 $m^2\ g^{-1}$, and notably, the S_{BET} of Pt nanoparticles in Pt–Mn_2O_3/CN further escalated to 31.94 $m^2\ g^{-1}$. This amplification can be primarily attributed to the incorporation of Mn_2O_3 species into the mid-layer of CN during the solvent heating process, thus fostering the creation of more medium-sized pores. Additionally, the appropriate distribution of Pt nanoparticles either evenly dispersed on the CN surface or bonded with Mn_2O_3 and CN further facilitates the formation of a mesoporous structure.[17] The past investigation underscores that

© 2024 The Author(s). Published by the Royal Society of Chemistry

Open Access Article. Published on 20 Januari 2024. Downloaded on 8/13/2025 6:22:11 AM.
This article is licensed under a Creative Commons Attribution-NonCommercial 3.0 Unported Licence.

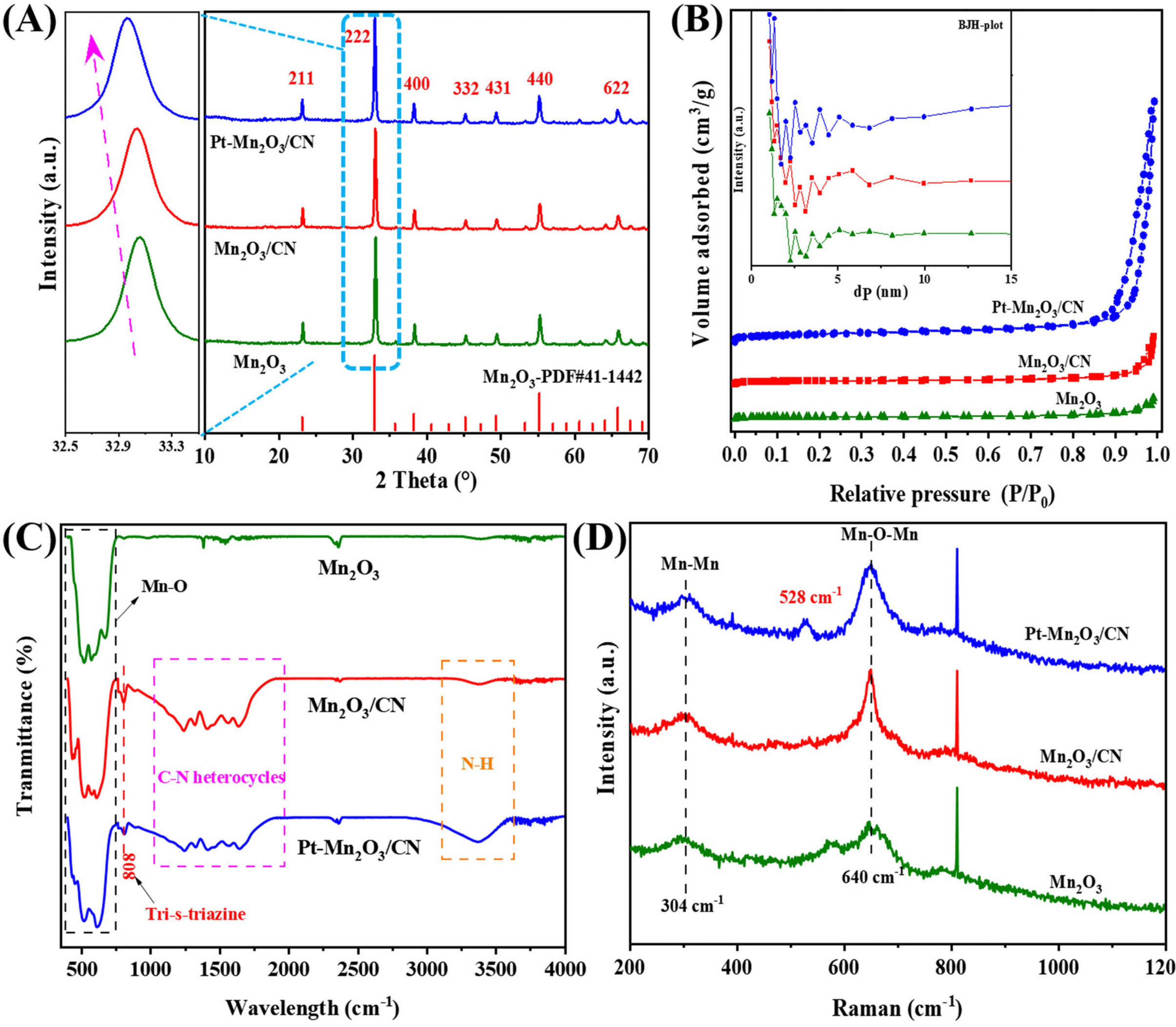

Fig. 1 (A) XRD patterns, (B) N_2 adsorption–desorption isotherm, (C) FTIR spectra, and (D) Raman spectra of different catalysts.

a larger specific surface area in the catalyst positively influences both the adsorption in catalytic reactions and the resultant catalytic activity.[22] The pore size distribution across all samples exhibited mesoporous characteristics, showcasing variations corresponding to the varying CN and Pt content. Notably, in Pt–Mn_2O_3/CN, the pore volume experienced a considerable reduction to 0.231 $cm^3\ g^{-1}$. CN possesses a π-conjugated aromatic system, a result of the sp^2 hybridization involving carbon and nitrogen atoms. This configuration allows CN to adsorb and activate reactant molecules sharing a similar conjugate aromatic structure, primarily through π–π interconnection.[23] Additionally, in π-delocalized electronic systems, significant delocalized p electrons become integrated with the lone pair electrons on loaded Pt atoms, thereby activating and fostering the formation of π–π interactions.[24] The introduction of an appropriate quantity of Mn_2O_3 facilitates the opening of the interlayer structure, leading to increased adsorption of toluene molecules. Consequently, Pt–Mn_2O_3/CN, characterized by a larger specific surface area (S_{BET}) and an increased π–π interaction proportionate to CN content, exhibits enhanced toluene adsorption capacity. This enhancement proves advantageous in augmenting the number of activated toluene molecules.

The FTIR spectra of the catalysts produced are presented in Fig. 1C. The infrared signal at 808 cm^{-1} corresponds to the

Table 1 BET and XPS element analysis of different catalysts

Catalysts	BET surface ($m^2\ g^{-1}$)	Total pore volume ($cm^3\ g^{-1}$)	Average pore diameter (nm)	Pt theoretical loading/(wt%)	ICP-Pt (wt%)	Mn^{4+}/Mn^{3+}
Mn_2O_3	11.01	0.267	41.21	—		0.49
Mn_2O_3/CN	17.68	0.282	51.51	—		0.51
Pt–Mn_2O_3/CN	31.94	0.231	28.97	0.4	0.3	0.58

© 2024 The Author(s). Published by the Royal Society of Chemistry

Open Access Article. Published on 20 Januari 2024. Downloaded on 8/13/2025 6:22:11 AM.
This article is licensed under a Creative Commons Attribution-NonCommercial 3.0 Unported Licence.

distinctive breathing mode associated with triazine rings in CN.[25] Peaks within the range of 1000–1950 cm^{-1} signify stretching vibration modes of C–N and C=N heterocycles, whereas those at 3000–3600 cm^{-1} indicate the stretching vibration of N–H. This is attributed to either insufficient condensed amino groups or remaining hydrogen atoms attached to the edges of graphite-like CN.[16] The peaks observed at 614 cm^{-1} and 514 cm^{-1} result from the asymmetric bending of Mn–O and the stretching vibration of O–Mn–O.[26] Beyond the analysis of the catalyst phase, Raman spectroscopy was employed to investigate the vibrational patterns of the catalyst's surface species. In Fig. 1D, the Raman peaks near 304 cm^{-1} and 640 cm^{-1} correspond to Mn–Mn and the E_g symmetric tensile vibration mode of Mn–O–Mn, respectively, primarily associated with the Jahn–Teller (J–T) distortion.[27] In these samples, the heightened peak intensity at 640 cm^{-1} serves as an indicator of increased J–T distortion. Notably, Pt–Mn_2O_3/CN exhibits the highest peak intensity, signifying the most pronounced ordering of the E_g electron orbit.[28] Raman spectra of Pt–Mn_2O_3/CN at 528 cm^{-1} are ascribed to the three Raman-active vibrations of δ (N–Pt–N), ν_s(Pt–N), and ν_{as}(Pt–N), respectively.[29]

To further elucidate the structure of Pt NPs, Mn_2O_3, and CN within Pt–Mn_2O_3/CN, we conducted a detailed microscopic analysis using transmission electron microscopy (TEM), displaying the findings in Fig. 2 and Fig. S3 (ESI†). Throughout the high-temperature and high-pressure treatment, the catalyst retained the layered configuration of CN, exhibiting a consistent flat and stacked sheet structure. Within this framework, Mn_2O_3 was found embedded, with bright white minuscule spots in Fig. 2A and G, indicating Pt NPs evenly distributed atop Mn_2O_3, bound to CN. The size distribution analysis of the Pt nanoparticles depicted in Fig. 2C revealed a range from 3.84 nm to 11.33 nm, with an average size of 6.37 nm. High-resolution TEM images in Fig. 2D–F revealed spherical bright spots corresponding to Pt NPs situated on the surface of Mn_2O_3. However, these images only exhibited lattice patterns specific to Mn_2O_3, with indexed lattice spacings of 0.38 nm for (211) planes and 0.19 nm for (422) planes in Mn_2O_3. Further examination *via* HRTEM (Fig. S4, ESI†) unveiled ultrafine nanoparticles adhered to CN, measuring approximately 6.0 nm in size. Enlarged sections in Fig. S4 (ESI†) delineated lattice fringe spacings of these ultrafine nanoparticles at approximately 0.22 nm, corresponding to the *d*-spacing observed in the (111) facets of cubic Pt.[30]

Additionally, the elemental distribution was visualized through energy-dispersive X-ray (EDX) spectroscopy, revealing separate dispersion of Mn and Pt on CN, and some Pt dispersed on Mn_2O_3 particles. The actual Pt loading in Pt–Mn_2O_3/CN was observed to be 1% lower than the theoretical loading (refer to Fig. S5, ESI,† and Table 1). This discrepancy can be attributed to the loss of some Pt in the ethanol solution during the solvent-thermal reaction. The bonding of Pt to metal oxides typically induces the separation and migration of photo-induced carriers, thereby enhancing the photocatalytic activity. Furthermore, the interaction between Pt and metal oxides serves to augment the presence of reactive oxygen species on the catalyst, facilitating catalytic reactions. Simultaneously, the uniform distribution of Pt nanoparticles on the surface of Mn_2O_3 bound to CN proves advantageous in capturing and utilizing photons across a broader wavelength spectrum. In the solvent-thermal synthesis process, we also synthesized the Pt–Mn_2O_3 catalyst. However, TEM analysis revealed that in the absence of CN as the dispersion carrier, Pt nanoparticles tend to agglomerate, as highlighted in the red box in Fig. S6 (ESI†). These stacked and agglomerated particles are detrimental to the overall efficiency of the catalyst.

Catalytic performance

The catalyst we prepared underwent testing for its photothermal catalytic oxidation activity under the entire solar spectrum with an illumination intensity of 300 mW cm^{-2}. In the static reaction conditions depicted in Fig. 3A and B, the photothermal removal percentage of toluene exhibited a specific order across different catalysts: Pt–Mn_2O_3/CN (99%) > Mn_2O_3/CN (53%) > Mn_2O_3 (45.5%) > Pt–CN (33.7%). Particularly noteworthy is the CO_2 yield achieved by Pt–Mn_2O_3/CN, reaching an impressive 80.9%, significantly surpassing Mn_2O_3/CN (11.2%), Pt–CN (10.4%) and Mn_2O_3 (6.5%). The introduction of Pt through doping notably enhances the overall catalytic efficiency in detoxifying toluene, converting it into CO_2 and H_2O. This enhancement is attributed to the improved dispersion of Pt nanoparticles and the increased specific surface area of the catalyst facilitated by CN-supporting materials. The underwhelming performance of Pt–CN underscores the pivotal role of Mn_2O_3 in catalytic conversion. To delve into the impact of Pt loading on catalytic efficacy, various catalysts with distinct Pt loadings were scrutinized, as illustrated in Fig. S7 (ESI†). The introduction of Pt markedly enhanced the catalytic performance; however, a subsequent increase in content to 1% led to a slight reduction in performance. This diminution could be ascribed to the potential agglomeration of surface Pt NPs.

To assess the enduring catalytic performance and practicality of Pt–Mn_2O_3/CN, we employed a custom-made stainless steel fixed bed continuous flow reactor for testing its photothermal catalytic activity against toluene. The reaction conditions comprised 200 ppm toluene, 20 vol% O_2, and N_2. The catalyst's weight hourly space velocity (WHSV) in the reactor was controlled at 30 000 mL g^{-1} h^{-1}, and we investigated the impact of H_2O and different light intensities on its stability. As depicted in Fig. 3C, once the reaction stabilized, the catalyst was not sufficiently activated at 200 and 250 mW cm^{-2} for 4 hours while the toluene conversion remained below 50%. When the light intensity was increased to 300 mW cm^{-2}, the toluene conversion reached 92.8% and remained stable with a consistent CO_2 yield of approximately 79.6%. Remarkably, even after 36 hours, the catalytic efficiency remained robust. Introducing 5 and 10 vol% H_2O into the reaction system led to a decline in catalytic performance, with the toluene conversion dropping to 85.1% and 74.6% while the CO_2 yield decreased to 71.8% and 62.4%. Typically, H_2O and CO_2 are byproducts of toluene oxidation, and hence, considering the reaction

© 2024 The Author(s). Published by the Royal Society of Chemistry

Open Access Article. Published on 20 Januwari 2024. Downloaded on 8/13/2025 6:22:11 AM.
This article is licensed under a Creative Commons Attribution-NonCommercial 3.0 Unported Licence.

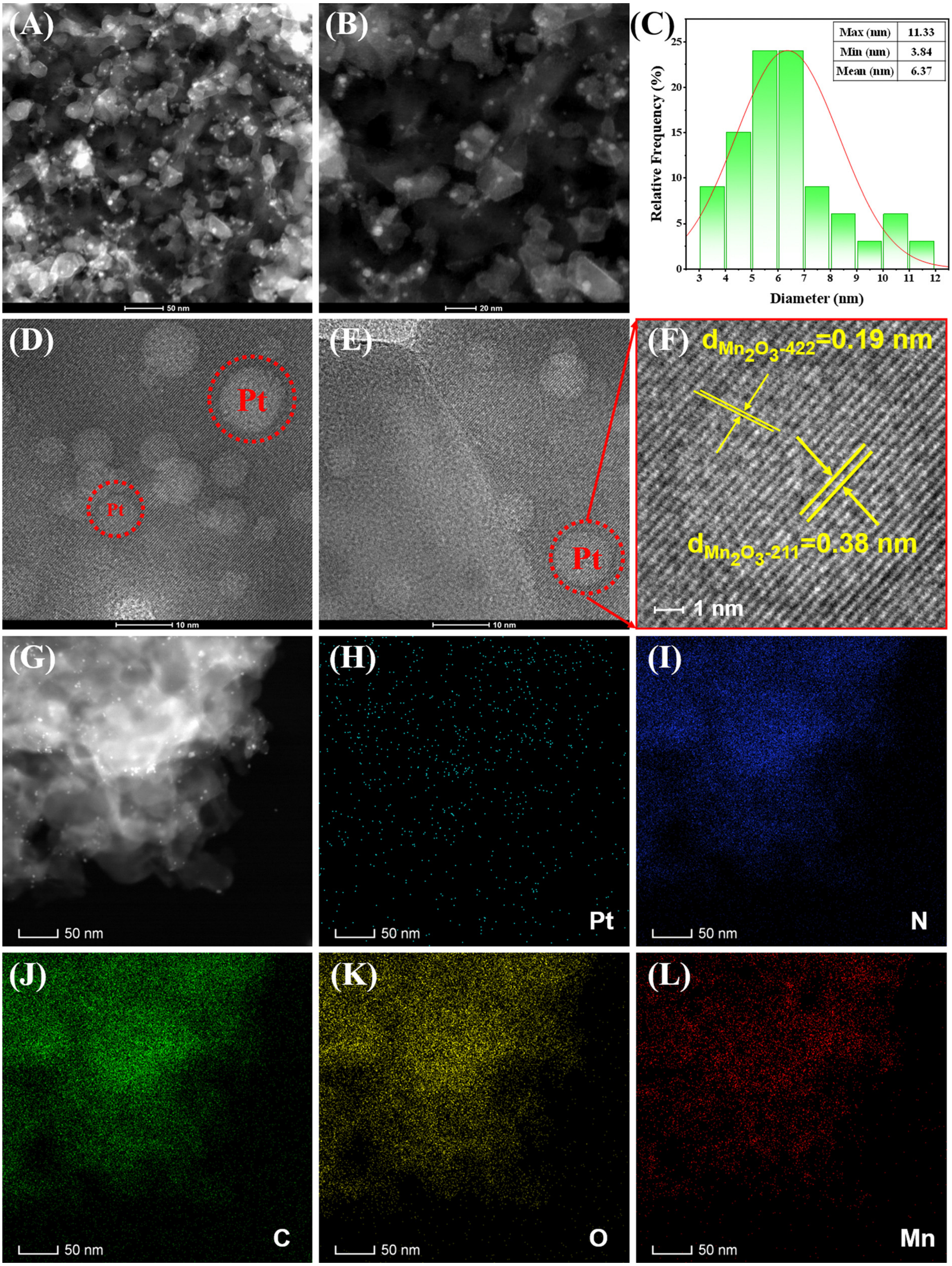

Fig. 2 (A) and (B) TEM images at different magnifications, (C) size distribution of the Pt NPs, (D) and (E) HRTEM images, (F) the shots of the selected area in the panel, (G)–(L) EDS phase mapping of the Pt (blue), O (yellow), Mn (red), N (navy), and C (green), distributions images of the Pt–Mn_2O_3/CN catalyst.

equilibrium, the introduction of water adversely affects the process.[31] Noteworthy is the swift recovery of toluene conversion and CO_2 yield upon the removal of water vapor, underscoring the excellent catalytic resilience of Pt–Mn_2O_3/CN

Open Access Article. Published on 20 Januari 2024. Downloaded on 8/13/2025 6:22:11 AM.
This article is licensed under a Creative Commons Attribution-NonCommercial 3.0 Unported Licence.

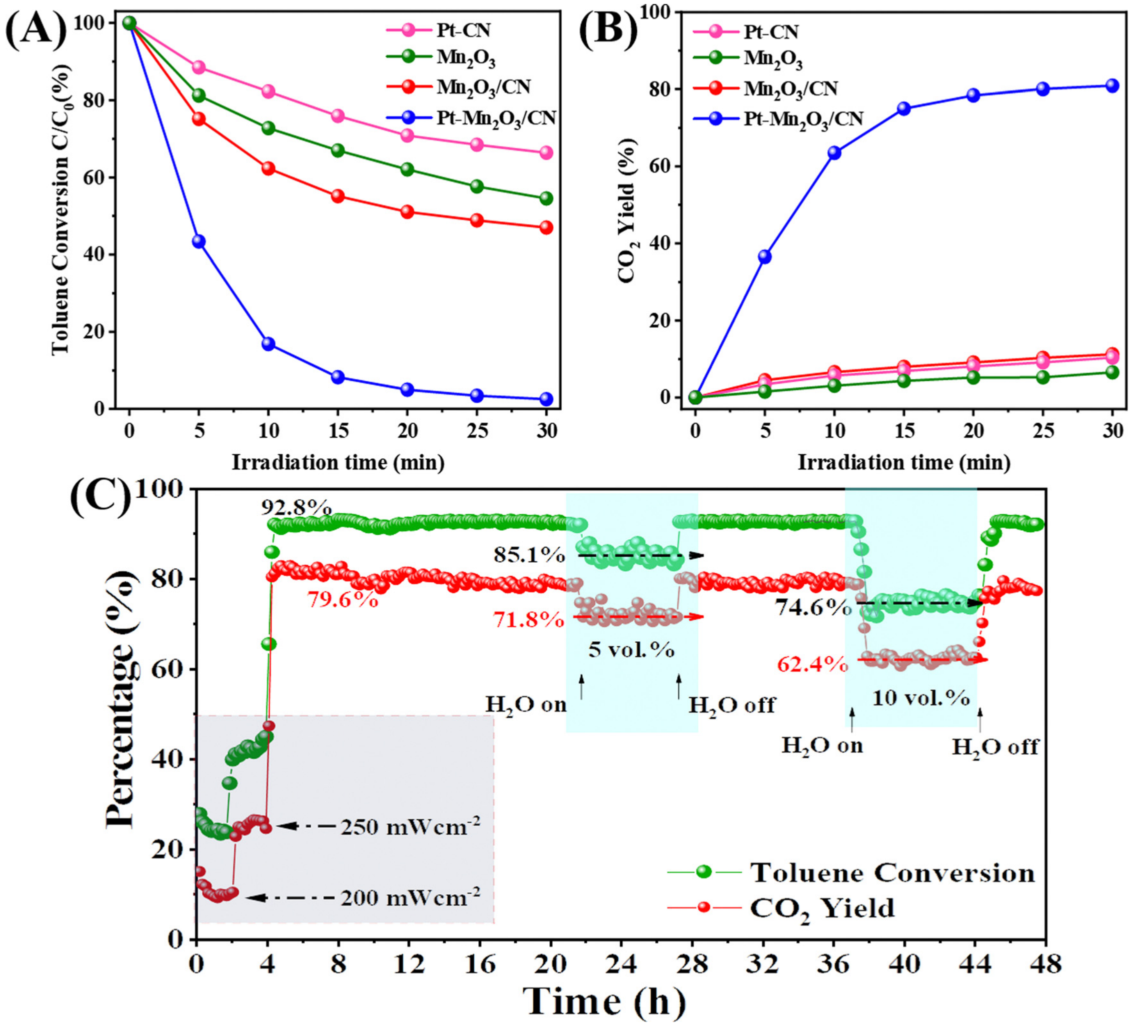

Fig. 3 Photothermal catalytic oxidation of toluene, (A) toluene conversion, and (B) CO_2 yield during the static reaction with 400 ppm toluene over the different catalysts, (C) toluene conversion and CO_2 yield during the continuous flow reaction over the Pt–Mn_2O_3/CN catalysts (full solar spectrum irradiation with 300 mW cm^{-2} light intensity, 200 ppm toluene, and WHSV = 30 000 mL g^{-1} h^{-1}).

to moisture. This underscores the catalyst's enduring performance under conditions simulating real exhaust scenarios.

Surface properties of the catalysts

The X-ray photoelectron spectroscopy (XPS) analysis of the C 1s spectra (Fig. 4A) reveals three distinct peaks at 284.8 eV, 285.8 eV, and 288.3 eV, corresponding to C–C bonds, C–NH_2 species, and carbon in N–C═N of the carbon nitride (CN), respectively.[16] Importantly, the peaks at 285.8 eV and 288.3 eV exhibit a shift towards higher binding energy compared to the C of CN, suggesting the presence of a chemical interaction between CN and Pt–Mn_2O_3. To further elucidate the origin of Pt and CN electron transfer, the Mn 2p spectra were analyzed (Fig. 4B). Given the various valence states of Mn on the catalyst surface, we focused on the three most common states (Mn^{2+}: ∼642.0 eV, Mn^{3+}: ∼642.6 eV, and Mn^{4+}: ∼644.1 eV).[32] Evidently, the surface Mn on all catalysts predominantly exists in the Mn^{3+} form (Mn^{3+} content >40%), aligning with the XRD results indicating the presence of Mn_2O_3. In Table 1, the incorporation of Pt nanoparticles led to an improvement in the surface Mn^{4+}/Mn^{3+} molar ratio, increasing from 0.49 to 0.58, signifying an enhanced concentration of surface Mn^{4+}. In simpler terms, loading Pt NPs resulted in an augmented surface oxygen vacancy concentration in Mn_2O_3/CN. Furthermore, compared to the pure Mn_2O_3 sample, all Pt–Mn_2O_3/CN catalysts displayed a higher binding energy of the Mn $2p_{3/2}$ peak, confirming the electron transfer from CN and Mn to Pt. Consequently, the XPS spectra of C 1s and Mn 2p affirm that the electronic coupling effect at the Pt–Mn_2O_3/CN interfacial active sites is more pronounced than that at the active sites of Mn_2O_3/CN.[33] This suggests that intercalating Mn_2O_3 and Pt nanoparticles into the lamellar CN induces structural defects, adjusts the electronic structure, and facilitates the generation of redox electric pairs of Mn^{4+}/Mn^{3+}.

Observing the data, it becomes apparent that samples exhibiting superior activity demonstrated a higher Mn^{4+}/Mn^{3+} molar ratio. The average valence state of Mn in Mn_2O_3 is +3. When an oxygen defect occurs, the Mn^{2+} content and Mn^{4+}

© 2024 The Author(s). Published by the Royal Society of Chemistry

Open Access Article. Published on 20 Januari 2024. Downloaded on 8/13/2025 6:22:11 AM.
This article is licensed under a Creative Commons Attribution-NonCommercial 3.0 Unported Licence.

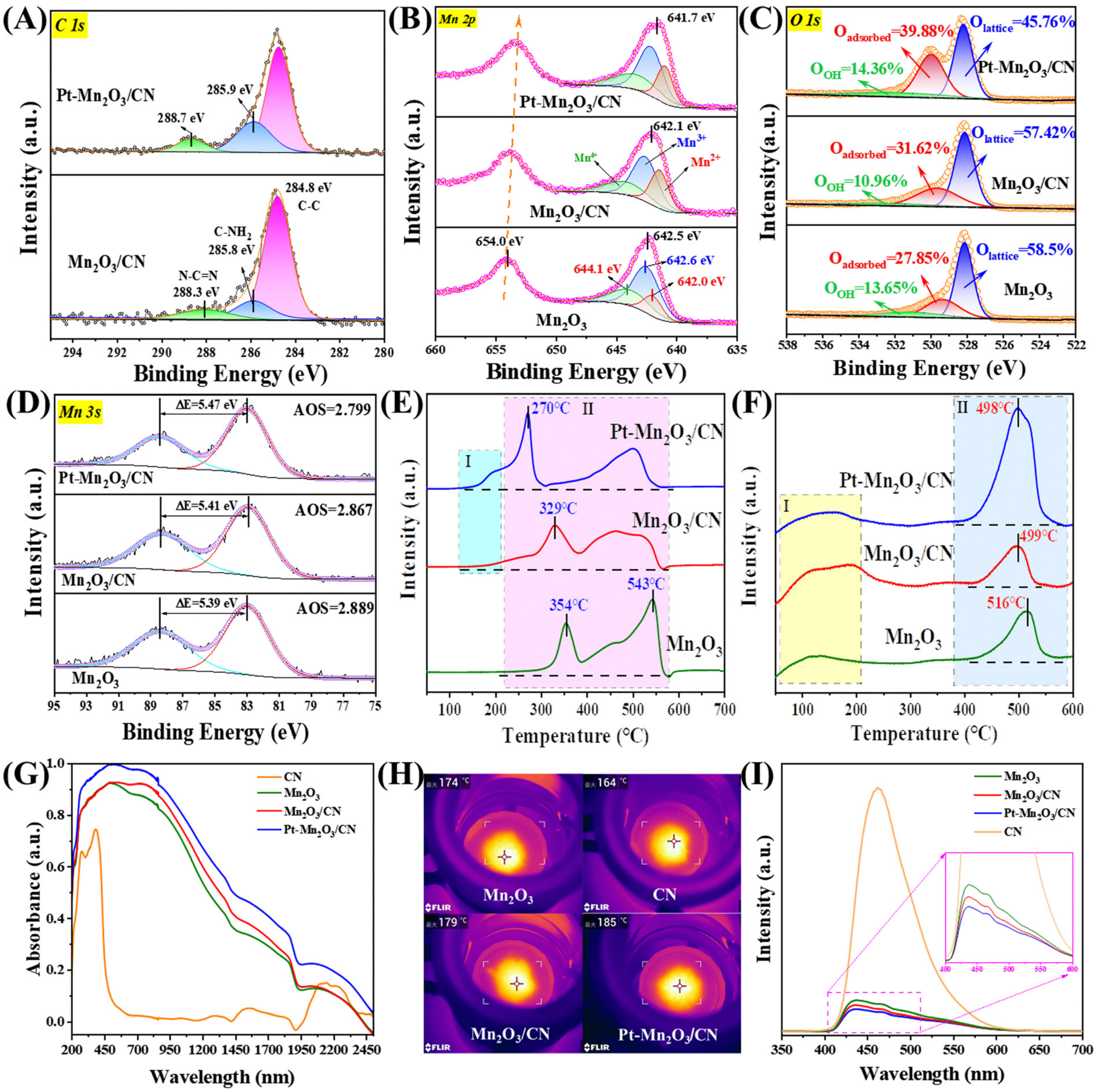

Fig. 4 XPS survey spectra of (A) C 1s, (B) Mn 2p, (C) O 1s, and (D) Mn 3s, (E) H_2-TPR, (F) O_2-TPD, (G) UV-Vis-IR absorption spectrum, (H) photothermal conversion temperatures and (I) photoluminescence spectra over different catalysts.

content must change to maintain the overall electron balance.[3,33,34] Following the incorporation of Pt NPs, a noticeable alteration in the valence distribution of various carriers occurred, aligning with the results of the activity assessment. This change followed the trend of high Mn^{4+} content correlating with excellent activity observed prior to loading. The outcomes of the peak separation analysis of O 1s orbitals, depicted in Fig. 4C, reveal that the asymmetrical O 1s spectrum of each sample can be deconstructed into three components at binding energies of 528.1, 529.4, and 531.4 eV. These correspond to surface lattice oxygen ($O_{lattice}$), adsorbed oxygen ($O_{adsorbed}$), and adsorbed water or carbonate species (O_{OH}).[35] Notably, in Table 1, the Pt–Mn_2O_3/CN sample exhibited the highest $O_{adsorbed}$ concentration (39.88%) among all samples, once again validating that a heightened $O_{adsorbed}$ concentration promotes toluene combustion. It is observed that carriers with higher Mn^{4+} content also displayed a higher oxygen content on their surface, consistent with the peak separation results of Mn 2p orbitals. Within this context, $O_{adsorbed}$ species play a pivotal role in catalytic degradation. Their effectiveness hinges on the presence of oxygen vacancies (O_{vs}) implanted in the catalysts. In essence, an increased number of oxygen vacancies translates to more surface-adsorbed active oxygen, ultimately leading to higher final degradation efficiency.

Moreover, the oxygen vacancy concentration can be represented by the average oxidation state (AOS) of Mn 3s in the Mn_2O_3 samples. The principle here is that a lower AOS value corresponds to a higher oxygen vacancy concentration.[36]

Open Access Article. Published on 20 Januari 2024. Downloaded on 8/13/2025 6:22:11 AM.
This article is licensed under a Creative Commons Attribution-NonCommercial 3.0 Unported Licence.

This calculation is derived from the multiplet splitting of Mn 3s orbitals, and it follows the formula outlined below:

$$\mathrm{AOS} = 8.98\text{–}1.13\Delta E_s\ (\mathrm{eV})$$

The ΔE_s, denoting the disparity in binding energy between the primary peak and its associated satellite arising from the multiplet splitting within Mn 3s orbitals, play a crucial role. The determined ΔE_s values for Mn_2O_3, Mn_2O_3/CN, and Pt–Mn_2O_3/CN stand at 5.39, 5.41, and 5.47 eV, respectively (refer to Fig. 4D). Notably, the Pt–Mn_2O_3/CN catalyst exhibits the lowest Average Oxidation State (AOS) among all counterparts, registering at 2.78, indicative of its heightened O_{vs} content, which is in line with EPR analysis (Fig. S8, ESI†). The escalation in oxygen vacancy concentration aligns with enhanced oxygen migration capability.[37] Within this spectrum, Pt–Mn_2O_3/CN manifests a substantial increase in oxygen vacancies, primarily attributed to the pronounced influence of strong metal–support interactions (SMSI) on the Mn–O bond within the carrier. This phenomenon results in the formation of additional oxygen vacancies, emerging as the principal factor contributing to the marked enhancement in its catalytic activity.[34]

The reduction performance of the catalyst was explored through H_2 temperature-programmed reduction (H_2-TPR). In Fig. 4E, the reduction spectrum of manganese oxides with diverse morphologies is depicted. The peaks around 354 °C signify the reduction from Mn^{4+} to Mn^{3+}, while those at approximately 543 °C indicate the reduction from Mn^{3+} to Mn^{2+}. The remaining high-temperature peaks are attributed to the partial reduction of the surface phase.[38] Typically, the temperature at which Mn_2O_3 transforms from Mn^{4+} to Mn^{3+} is employed to assess the reduction capacity of Mn_2O_3.[39] It is evident from the analysis that the Pt-loaded sample exhibits superior low-temperature reducibility. Region I represents the reduction absorption peak of Pt–Mn_2O_3/CN and surface-adsorbed oxygen, while Region II corresponds to the Mn_2O_3 reduction absorption peak. Despite the extremely low Pt loading, even if all Pt oxides exist in the form of PtO_2, it remains significantly lower than the hydrogen consumption in Region I. Consequently, the absorption peak in Region I is predominantly ascribed to the hydrogen overflow effect induced by strong metal–support interaction (SMSI). This prompts the Mn_2O_3/CN surface oxygen species near Pt NPs to react with H_2.[34] The absorption peak in Region II reveals that the $Mn^{4+} \rightarrow Mn^{3+}$ reduction peak intensity of the Pt–Mn_2O_3/CN sample is the highest, with the lowest reduced temperature. This suggests that Pt–Mn_2O_3/CN exhibits superior low-temperature oxidizability, heightened surface oxygen mobility, an abundance of reactive oxygen species, and a greater ability to accept electrons compared to Mn_2O_3.

Oxygen temperature-programmed desorption (O_2-TPD) analysis was conducted to discern the oxygen species within Mn_2O_3 and investigate potential factors influencing its oxidation properties. The results of the analysis are depicted in Fig. 4F. The desorption peak in the range of 50–200 °C was ascribed to the release of surface-adsorbed oxygen (peroxide species, O_2^-), while the peak at 400–600 °C was associated with the desorption of surface lattice oxygen (monatomic species, O^-). Furthermore, the desorption peak exceeding 600 °C was attributed to the release of bulk lattice oxygen (O^{2-} species).[10] Considerable attention has been directed towards the first two peaks, as lattice oxygen species (O^{2-} species, >550 °C) tend to become inert during toluene oxidation at low temperatures.[40] The diagram illustrates that the order of surface active lattice oxygen content among the three samples is Pt–Mn_2O_3/CN $>$ Mn_2O_3/CN $>$ Mn_2O_3. Notably, the content of surface lattice oxygen (monatomic species, O^-) has a pronounced positive impact on high efficiency and low-temperature oxidation. This observation is attributed to the catalyst's surface lattice oxygen being the primary substance adsorbed by the activated carrier during low-temperature oxidation. The migration of oxygen to replenish the consumed surface lattice oxygen after oxygen vacancy activation can further mineralize the activated toluene, indicating superior oxygen mobility.

Photothermal catalysis involves the utilization of light energy to transform it into heat energy during a chemical reaction. This process enhances the efficiency and speed of catalytic reactions by absorbing and converting light energy into heat.[41] The initial step in photothermal catalysis is light absorption, a crucial determinant of how much light energy the catalyst absorbs. Catalysts that can absorb light across a broader range of wavelengths generally exhibit superior catalytic performance because they can harness a more extensive portion of the solar energy spectrum. The Pt–Mn_2O_3/CN sample, as depicted in Fig. 4G, displays a notable photoresponse in the ultraviolet to visible and near-infrared (IR) spectral regions (up to 2500 nm), confirming its exceptional solar absorption capacity. Comparing the absorption spectra intensities of different samples, the order is Pt–Mn_2O_3/CN $>$ Mn_2O_3/CN $>$ Mn_2O_3 $>$ CN. Furthermore, the photothermal conversion temperature is critical, as it denotes the temperature at which the heat energy generated by light absorption elevates the temperature of both the catalyst and the reactants. The increase in temperature can accelerate the reaction rate, improve the selectivity of the reaction, or enable the reaction to take place under milder conditions. Infrared thermography was employed to assess the equilibrium temperatures of various catalysts under light irradiation, revealing that the Pt–Mn_2O_3/CN sample exhibited the best catalytic performance with the highest surface temperature at 185 °C (Fig. 4H). Kirchhoff's law posits that the infrared (IR) emissivity is equal to the IR absorptivity of a material in thermodynamic equilibrium. Consequently, the Pt–Mn_2O_3/CN's IR absorption results in robust IR radiation, leading to intense thermal radiation diffusion.[42] Moreover, Pt nanoparticles uniformly dispersed on the catalyst surface produce a plasmonic resonance effect under light, which enhances the light absorption and photothermal conversion efficiency.[43]

Under 280 nm excitation light, the singular Mn_2O_3 demonstrates a pronounced photoluminescence (PL) intensity attributable to substantial photogenerated charge recombination. In contrast, the Pt–Mn_2O_3/CN composite exhibits a markedly diminished PL intensity (Fig. 4I), suggesting the timely

© 2024 The Author(s). Published by the Royal Society of Chemistry

Open Access Article. Published on 20 Januari 2024. Downloaded on 8/13/2025 6:22:11 AM.
This article is licensed under a Creative Commons Attribution-NonCommercial 3.0 Unported Licence.

migration of photogenerated electrons from Mn_2O_3 to Pt nanoparticles, effectively suppressing charge recombination. Likewise, Mn_2O_3/CN displays a reduction in fluorescence intensity, albeit less pronounced than the Pt–Mn_2O_3/CN catalyst scenario. This disparity may stem from the lower Mn_2O_3 decoration content on CN, making the migration of photogenerated holes comparatively more challenging than that of electrons. These outcomes underscore the superior efficiency of the Pt–Mn_2O_3/CN co-catalyst and heterojunction synergy over single modifications, aligning with the overall enhancement observed in photothermal catalytic performance.

The probable mechanism involved in the photothermal degradation of toluene

An in-depth exploration of the mechanisms underlying toluene oxidation led us to conduct *in situ* diffuse reflection infrared Fourier transform spectroscopy (DRIFTS) measurements under specific conditions. Employing the typical reaction setup, Fig. 5A presents *in situ* DRIFTS spectra recorded at different temperatures. Prior to the measurement, the catalyst underwent pretreatment under an N_2 flow (30 mL min^{-1}) at 300 °C for 30 minutes. Subsequently, the system was cooled down to 100 °C, and the background spectra were collected.

The peak at 1177 cm^{-1} is unequivocally identified as a C–O stretching vibration mode distinctive of alkoxide species. This implies that the adsorbed toluene can engage with the catalyst by cleaving the C–H bond of the methyl group (–CH_4) to generate benzyl alcohol.[16] The vibrational band at 1300 cm^{-1} is assigned to the maleic anhydride species, while the emergence of the band at 1364 cm^{-1}, due to the symmetrical deformation vibration of the methyl group, signifies the

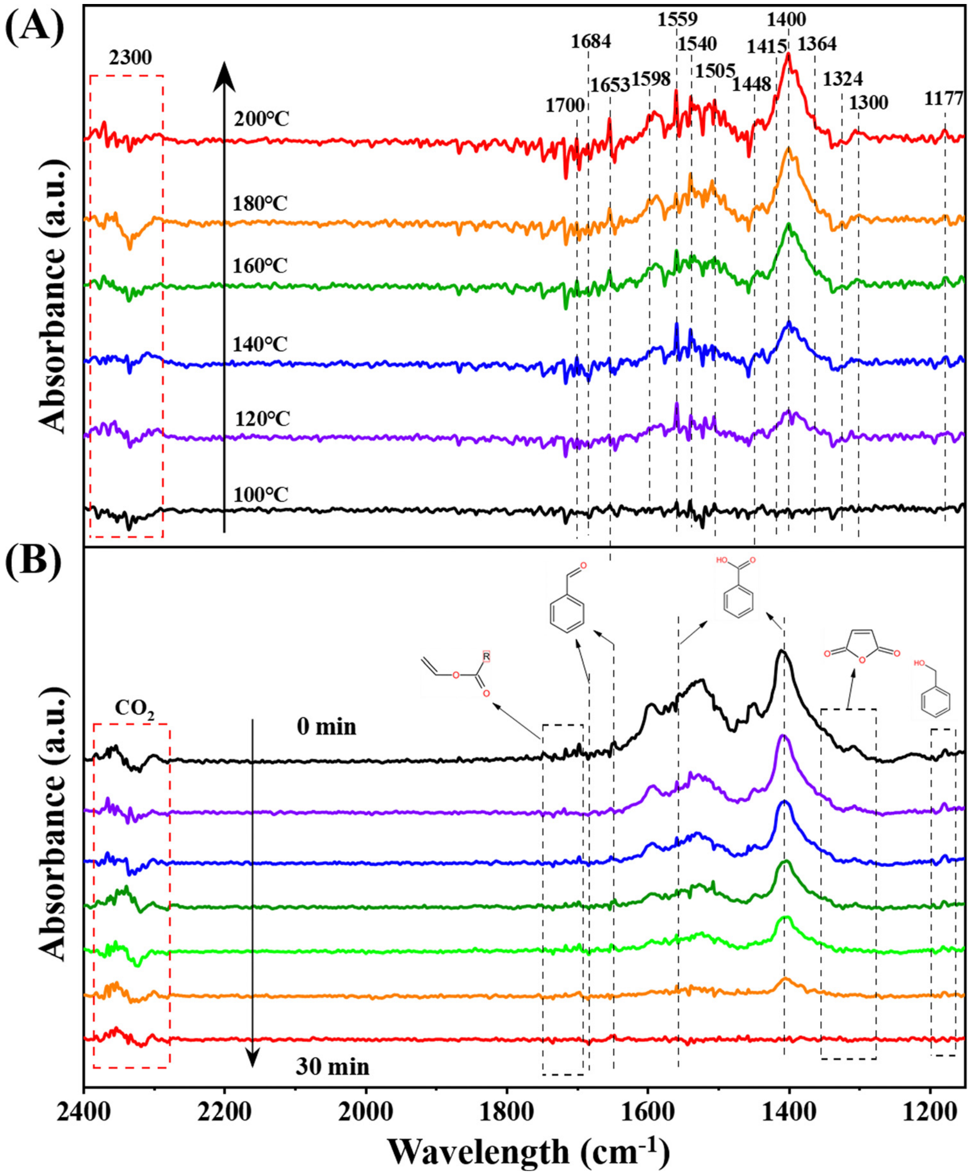

Fig. 5 *In situ* DRIFTS spectra of (A) toluene adsorption at different temperatures and (B) toluene oxidation (1000 ppm toluene + O_2 + N_2 feed gas) over Pt–Mn_2O_3/CN.

Open Access Article. Published on 20 Januwari 2024. Downloaded on 8/13/2025 6:22:11 AM.
This article is licensed under a Creative Commons Attribution-NonCommercial 3.0 Unported Licence.

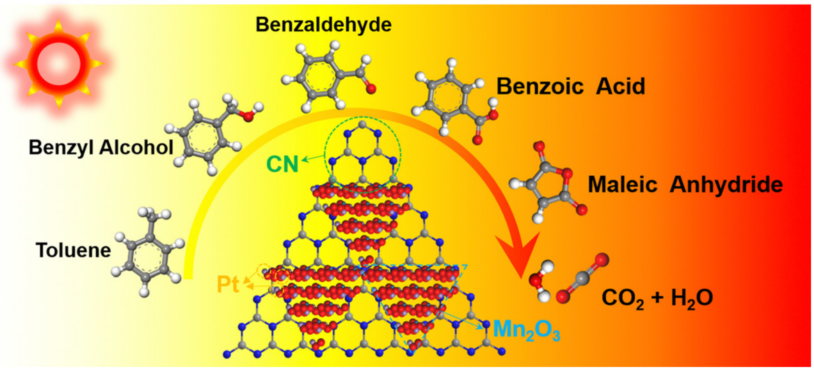

Fig. 6 Scheme of toluene oxidation over Pt–Mn_2O_3/CN.

formation of acetone.[44] The peaks at 1448 cm^{-1} and 1598 cm^{-1} are ascribed to the vibrational mode of C═C in the benzene ring.[45] Furthermore, the vibrational bands at 1415 cm^{-1} and 1540 cm^{-1} are segregated into the C–O symmetry of benzoate and antisymmetry modes.[17] The bands at 1559 cm^{-1} and 1400 cm^{-1} are indicative of carboxylic acid groups (1559 cm^{-1} representing asymmetric $-COO^-$ tensile vibration, and 1400 cm^{-1} representing symmetric $-COO^-$ tensile vibration), suggesting the formation of benzoate species.[46] Bands situated at 1598 cm^{-1} and 1505 cm^{-1} are associated with the in-plane skeleton vibration of the aromatic ring.[34] Additionally, bands at 1684 cm^{-1} and 1653 cm^{-1} are attributed to the C═O stretching vibration,[47] while the band at 1324 cm^{-1} corresponds to an aldehyde group consisting of skeletal C–C stretching vibration, suggesting the formation of benzaldehyde species.[7] The multiple signal peaks in the range of 1668–1700 cm^{-1} can be categorized as C═C tensile vibration in vinyl acetate. Notably, characteristic bands (2300–2340 cm^{-1}) of adsorbed CO_2 are also discerned, and their intensities escalate with an increase in the reaction temperature.[46]

Examining the spectra reveals a discernible trend where intermediate species are progressively amassed and depleted during the adsorption and oxidation of toluene. In the course of toluene heating and adsorption, the Pt–Mn_2O_3/CN catalyst exhibited peaks of intermediate species on the surface, and the peak intensity demonstrated an increase. This suggests the involvement of surface lattice oxygen from the catalyst in the oxidation process. When toluene adsorption was halted, and only oxygen was introduced (Fig. 5B), the intermediate species on the catalyst surface underwent continuous oxidation, leading to a gradual reduction in peak intensity. This phenomenon can be attributed to the activation of surface O_2 molecules, facilitating the profound oxidation of intermediates by reactive oxygen species. Nevertheless, the examination of *in situ* infrared spectra for pristine Mn_2O_3 reveals only a marginal alteration in the signal intensity of benzoic acid with no discernible progression to subsequent stages (Fig. S9, ESI†). This observation underscores the difficulty of activating reactive oxygen species on the surface of Mn_2O_3.

In the context of incomplete toluene combustion, the Pt–Mn_2O_3/CN catalyst surface displayed peaks corresponding to benzyl alcohol, benzaldehyde, benzoic acid, vinyl acetate, and maleic anhydride. Analyzing *in situ* DRIFTS spectrum data, the degradation pathway of toluene on Pt–Mn_2O_3/CN aligns with the illustrated route in Fig. 6. A hydrogen atom within the methyl group of toluene is eliminated, giving rise to benzyl alcohol. Subsequently, benzyl alcohol is subject to additional oxidation mediated by reactive oxygen species, leading to the sequential formation of benzaldehyde and then benzoic acid. This oxidative process further disrupts the structural stability of the benzene ring. Following this, the activated benzene ring and the carboxyl group undergo an attack, culminating in the generation of maleic anhydride. Ultimately, maleic anhydride undergoes conversion into carbon dioxide (CO_2) and water (H_2O).

Conclusion

In summary, harnessing renewable solar energy through photothermal catalysis presents a promising alternative to remediating VOCs. The approach involving Mn_2O_3 as the photothermal conversion center, CN as a uniformly dispersed medium for Pt nanoparticles, and Pt as the active site has proven successful. The loading of an appropriate proportion of Pt nanoparticles significantly enhanced the photothermal catalytic degradation activity of the Pt–Mn_2O_3/CN nanocomposite catalyst on toluene. This improvement is primarily attributed to the Pt nanoparticles inducing numerous oxygen vacancies in the catalyst, enhancing the oxygen adsorption content and surface fluidity, and activating the absorbed oxygen on the catalyst's surface. The effective utilization of sunlight for VOC degradation highlights its potential as a clean and renewable energy source, offering substantial environmental benefits.

Experimental

Chemical reagents

Manganous acetate tetrahydrate ($C_4H_6MnO_4{\cdot}4H_2O$), and platinum tetra ammonia nitric acid ($H_{12}N_6O_6Pt$) were purchased from Aladdin Reagents (Shanghai) Co., Ltd. Melamine ($C_3H_6N_6$) and glycol ($C_2H_6O_2$) were purchased from Sinopharm Chemical Reagent Co., Ltd. All these chemicals were of analytical grade and used without further purification.

© 2024 The Author(s). Published by the Royal Society of Chemistry

Open Access Article. Published on 20 Januari 2024. Downloaded on 8/13/2025 6:22:11 AM.
This article is licensed under a Creative Commons Attribution-NonCommercial 3.0 Unported Licence.

Catalyst preparation

Synthesis of the CN. A total of 2 g of melamine ($C_3H_6N_6$) powder underwent calcination at 550 °C for 4 hours (at a rate of 5 °C min^{-1}) within an alumina crucible. Subsequently, the resulting yellow product was meticulously ground into a powder for subsequent treatment.

Synthesis of the Pt–Mn_2O_3/CN. 3.6 g of $Mn(CH_3COO)_2·4H_2O$ and 1.8 g of pre-synthesized CN were dispersed in 480 mL of glycol, forming an aqueous dispersion. To this, (5.79 mL) of $H_{12}N_6O_6Pt$ (4 g L^{-1}) was introduced. The mixture was continuously stirred at 25 °C for 30 minutes, followed by transfer to an autoclave and heating at 180 °C for 10 hours. Post-reaction, the resulting precipitate underwent ethanol washing and subsequent drying for 8 hours at 60 °C. The resultant material underwent air-baking at 500 °C for 2 hours (heating rate: 5 °C min^{-1}). The resulting catalysts were designated as Pt–Mn_2O_3/CN, with Pt theoretical loading contents of 0.4 wt% (refer to Table 1).

In parallel, Mn_2O_3 and Mn_2O_3/CN were synthesized using the same aforementioned procedure, omitting $H_{12}N_6O_6Pt$.

Characterization

The X-ray diffraction (XRD) patterns of the catalysts were acquired employing a Bruker D8 Advance X-ray diffractometer (Bruker, Germany) with Cu Kα radiation (λ = 1.542 Å). BET adsorption and desorption isotherms were conducted using a Belsorp-Mini II analyzer (Japan). Fourier transform infrared spectroscopy (FTIR) data were obtained using a Nicolet Nexus 410 spectrometer. The Laser Raman spectrum was measured using an Ar ion laser as the excitation source, covering a frequency range of about 50–1400 cm^{-1} (HORIBA Jobin Yvon S.A.S.). X-ray photoelectron spectroscopy (XPS) analyses were executed within an ultrahigh vacuum chamber at room temperature, maintaining a pressure of 2×10^{-9} bar (Thermo Fisher Scientific, ESCALAB 250). The morphology and microstructures of the catalyst were scrutinized through transmission electron microscopy (TEM) (FEI Talos F200X) and scanning electron microscopy (SEM) (Hitachi, model SU1510). Gas chromatography (GC, Agilent Technologies 7890A) was employed to monitor the concentration of toluene and CO_2 during the catalytic process, while gas chromatography–mass spectrometry (GC-MS, Agilent Technologies 7890A-5975C) was utilized to identify specific components in the reactor. Furthermore, H_2-TPR and O_2 temperature-programmed desorption (O_2-TPD) analyses were conducted on the MicrotracBEL BELCAT-II chemical adsorption analyzer. EPR spectra were obtained through an electron *para*-magnetic resonance spectrometer (Bruker A300). A UV-Vis-IR spectrophotometer (UV-3600 plus) was employed to record the full-spectrum light absorption on the catalysts. The photoluminescence (PL) spectra were measured using a Hitachi F4500 fluorescence spectrophotometer with an excitation wavelength of 280 nm at room temperature.

In situ DRIFTS experiments were conducted using a Nicolet 50 spectrometer (Thermo Fisher, USA) equipped with a Harrick DRIFTS cell and an MCT/A detector. To perform time-dependent *in situ* DRIFTS, the catalyst underwent pretreatment under a nitrogen (N_2) flow at a rate of 30 mL min^{-1}, maintaining a temperature of 300 °C for 30 minutes. Subsequently, the system was cooled to 200 °C, and the background spectrum was recorded. Introducing 1000 ppm of toluene (at a flow rate of 10 mL min^{-1}) into the system occurred over 1 hour, followed by N_2 purging (at a flow rate of 30 mL min^{-1}) for 30 minutes to eliminate weakly adsorbed toluene. The sample was then subjected to a reaction at 200 °C under an air flow containing 21% O_2 in N_2. Concurrently, spectral data were collected throughout the entire process.

Photothermal catalytic activity

The photothermal catalytic oxidation of toluene was systematically investigated through both static and continuous flow reaction modes. The static reaction test, chosen for its capacity to elucidate the temporal evolution of intermediates, provides valuable insights into the mechanistic intricacies of the process. Concurrently, the continuous flow reaction test serves as a comprehensive evaluation of the catalyst's stability and practical efficacy under dynamic conditions.

For a detailed exposition of the catalytic performance experiments conducted on the aforementioned catalysts, we direct the reader to the ESI,† accompanying this manuscript.

Conflicts of interest

There are no conflicts to declare.

Acknowledgements

The authors gratefully acknowledge the financial support from the National Natural Science Foundation of China (22072170, U23A20125), the Zhejiang Provincial Key Research and Development Program (2021C03170), and the Ningbo Science and Technology Bureau (2019B10096).

References

1 Y. Yang, S. H. Zhao, L. F. Cui, F. K. Bi, Y. N. Zhang, N. Liu, Y. X. Wang, F. D. Liu, C. He and X. D. Zhang, *Green Energy Environ.*, 2023, **8**, 654–672.

2 B. Liu, J. Ji, B. Zhang, W. Huang, Y. Gan, D. Y. C. Leung and H. Huang, *J. Hazard. Mater.*, 2022, **422**, 126847.

3 X. Yu, B. H. Deng, L. X. Yang, M. L. Zou, Z. L. Chen, Y. X. Fan, Z. H. Wei, K. Chen, M. X. Lu, T. T. Ying, J. Zhang and W. L. Dai, *J. Environ. Chem. Eng.*, 2022, **10**(5), 108496.

4 C. Song, Z. Wang, Z. Yin, D. Xiao and D. Ma, *Chem. Catal.*, 2022, **2**, 52–83.

5 J.-J. Li, S.-C. Cai, E.-Q. Yu, B. Weng, X. Chen, J. Chen, H.-P. Jia and Y.-J. Xu, *Appl. Catal., B*, 2018, **233**, 260–271.

6 E. A. Elimian, M. Zhang, J. Chen, H. Jia, Y. Sun and J. He, *Appl. Catal., B*, 2022, **307**, 121203.

© 2024 The Author(s). Published by the Royal Society of Chemistry

Open Access Article. Published on 20 Januwari 2024. Downloaded on 8/13/2025 6:22:11 AM.
This article is licensed under a Creative Commons Attribution-NonCommercial 3.0 Unported Licence.

7 M. Zhang, G. Li, Q. Li, J. Chen, E. A. Elimian, H. Jia and H. He, *Environ. Sci. Technol.*, 2023, **57**, 4286–4297.

8 X. Li, Y. Wang, D. Chen, N. Li, Q. Xu, H. Li, J. He and J. Lu, *Green Energy Environ.*, 2023, **8**, 538–547.

9 Y. Park, V. N. Pham, K. Lee and H. Lee, *Inorg. Chem.*, 2023, **62**, 13428–13434.

10 X. Yu, M. Shi, Y. Fan, L. Yang, J. Zhang, W. Liu, W. Dai, S. Zhang, L. Zhou, X. Luo and S. Luo, *Appl. Catal., B*, 2022, **309**, 121236.

11 W. Zhao, M. Adeel, P. Zhang, P. Zhou, L. Huang, Y. Zhao, M. A. Ahmad, N. Shakoor, B. Lou, Y. Jiang, I. Lynch and Y. Rui, *Environ. Sci.: Nano*, 2022, **9**, 61–80.

12 T. Pan, H. Deng, Y. Lu, J. Ma, L. Wang, C. Zhang and H. He, *Environ. Sci. Technol.*, 2023, **57**, 1123–1133.

13 G. Chen, F. Wei, Z. Zhou, B. Su, C. Yang, X. F. Lu, S. Wang and X. Wang, *Sustainable Energy Fuels*, 2023, **7**, 381–388.

14 Q. Wang, G. Zhang, W. Xing, Z. Pan, D. Zheng, S. Wang, Y. Hou and X. Wang, *Angew. Chem., Int. Ed.*, 2023, **62**(25), e202303486.

15 M. Liu, G. Zhang, X. Liang, Z. Pan, D. Zheng, S. Wang, Z. Yu, Y. Hou and X. Wang, *Angew. Chem., Int. Ed.*, 2023, **62**(11), e202217448.

16 M. Zhang, S. Cai, J. Li, E. A. Elimian, J. Chen and H. Jia, *J. Hazard. Mater.*, 2021, **412**, 125266.

17 M. Zhang, H. Gao, J. Chen, E. A. Elimian and H. Jia, *Appl. Catal., B*, 2022, **307**, 121208.

18 J. Zhao, J. Liu, Z. Li, K. Wang, R. Shi, P. Wang, Q. Wang, G. I. N. Waterhouse, X. Wen and T. Zhang, *Nat. Commun.*, 2023, **14**(1), 1909.

19 J. Zhao, Y. Bai, Z. Li, J. Liu, W. Wang, P. Wang, B. Yang, R. Shi, G. I. N. Waterhouse, X. D. Wen, Q. Dai and T. Zhang, *Angew. Chem., Int. Ed.*, 2023, **62**(13), e202219299.

20 P. Niu, L. Zhang, G. Liu and H.-M. Cheng, *Adv. Funct. Mater.*, 2012, **22**, 4763–4770.

21 X. Zhang, X. Lv, F. Bi, G. Lu and Y. Wang, *Mol. Catal.*, 2020, **482**, 110701.

22 C. Kaewbuddee, P. Chirawatkul, K. Kamonsuangkasem, N. Chanlek and K. Wantala, *Chem. Eng. Commun.*, 2021, **209**, 512–528.

23 P. Yang, H. Ou, Y. Fang and X. Wang, *Angew. Chem., Int. Ed.*, 2017, **56**, 3992–3996.

24 I. A. Abdelhafeez, J. Chen and X. Zhou, *Sep. Purif. Technol.*, 2020, **250**, 117085.

25 W. Zhao, J. Wang, R. Yin, B. Li, X. Huang, L. Zhao and L. Qian, *J. Colloid Interface Sci.*, 2020, **564**, 28–36.

26 Q. Huang, X. Cai, M. Chen, Q. Yang, S. Fan, Y. Zhang, H. Hu, T. Gan and Z. Huang, *Chem. Eng. J.*, 2022, **436**, 135258.

27 Z. Xiao, F. Xia, L. Xu, X. Wang, J. Meng, H. Wang, X. Zhang, L. Geng, J. Wu and L. Mai, *Adv. Funct. Mater.*, 2021, **32**(14), 2108244.

28 X. Liu, J. Mi, L. Shi, H. Liu, J. Liu, Y. Ding, J. Shi, M. He, Z. Wang, S. Xiong, Q. Zhang, Y. Liu, Z. S. Wu, J. Chen and J. Li, *Angew. Chem., Int. Ed.*, 2021, **60**, 26747–26754.

29 M. S. Brogan, T. J. Dines and J. A. Cairns, *J. Chem. Soc., Faraday Trans.*, 1994, **90**, 1461–1466.

30 J. Xiao, C. Chen, S. Chen, H. Liu and T. Peng, *Chem. Eng. J.*, 2021, **425**, 131627.

31 J. Li, M. Zhang, E. A. Elimian, X. Lv, J. Chen and H. Jia, *Chem. Eng. J.*, 2021, **412**, 128560.

32 D. Zhang, J. Cao, X. Zhang, N. Insin, S. Wang, J. Han, Y. Zhao, J. Qin and Y. Huang, *Adv. Funct. Mater.*, 2021, **31**(14), 2009412.

33 H. Yan, S. Yao, J. Wang, S. Zhao, Y. Sun, M. Liu, X. Zhou, G. Zhang, X. Jin, X. Feng, Y. Liu, X. Chen, D. Chen and C. Yang, *Appl. Catal., B*, 2021, **284**, 119803.

34 Z. Xu, S. Mo, Y. Li, Y. Zhang, J. Wu, M. Fu, X. Niu, Y. Hu and D. Ye, *Chemosphere*, 2022, **286**, 131754.

35 X. Fu, Y. Liu, J. Deng, L. Jing, X. Zhang, K. Zhang, Z. Han, X. Jiang and H. Dai, *Appl. Catal., A*, 2020, **595**, 117509.

36 S. Fang, Y. Li, Y. Yang, J. Chen, H. Liu and X. Zhao, *Environ. Sci.: Nano*, 2017, **4**, 1798–1807.

37 C. Feng, F. Jiang, G. Xiong, C. Chen, Z. Wang, Y. Pan, Z. Fei, Y. Lu, X. Li, R. Zhang and Y. Liu, *Chem. Eng. J.*, 2023, **451**, 138868.

38 Z. Xie, Z. Lyu, J. Wang, A. Li and P. François-Xavier Corvini, *Chem. Eng. J.*, 2022, **429**, 132299.

39 H. Yan, Q. Shen, Y. Sun, S. Zhao, R. Lu, M. Gong, Y. Liu, X. Zhou, X. Jin, X. Feng, X. Chen, D. Chen and C. Yang, *ACS Catal.*, 2021, **11**, 6371–6383.

40 X. Yu, Z. Chen, Z. Wei, K. Chen, Y. Fan, M. Zou, X. Si, B. Deng, L. Yang and J. Zhang, *Funct. Mater. Lett.*, 2022, **15**(05), 2251042.

41 B. Su, Y. Kong, S. Wang, S. Zuo, W. Lin, Y. Fang, Y. Hou, G. Zhang, H. Zhang and X. Wang, *J. Am. Chem. Soc.*, 2023, **145**, 27415–27423.

42 Y. Li, J. Hao, H. Song, F. Zhang, X. Bai, X. Meng, H. Zhang, S. Wang, Y. Hu and J. Ye, *Nat. Commun.*, 2019, **10**, 2359.

43 S. C. Cai, J. J. Li, E. Q. Yu, X. Chen, J. Chen and H. P. Jia, *ACS Appl. Nano Mater.*, 2018, **1**, 6368–6377.

44 Z. Wang, H. Yang, R. Liu, S. Xie, Y. Liu, H. Dai, H. Huang and J. Deng, *J. Hazard. Mater.*, 2020, **392**, 122258.

45 E. Yu, J. Li, J. Chen, J. Chen, Z. Hong and H. Jia, *J. Hazard. Mater.*, 2020, **388**, 121800.

46 Z. Wang, S. Xie, Y. Feng, P. Ma, K. Zheng, E. Duan, Y. Liu, H. Dai and J. Deng, *Appl. Catal., B*, 2021, **298**, 120612.

47 Y. Shen, J. Deng, L. Han, W. Ren and D. Zhang, *Environ. Sci. Technol.*, 2022, **56**, 10433–10441.

© 2024 The Author(s). Published by the Royal Society of Chemistry